

Small angle X-ray scattering study for investigating 3D nanoparticle packing structure of Pt catalyst on Gd-doped CeO₂ supports for fuel cells

Tomoyuki Iwata*, Kazuhiko Omote* and Katsuyoshi Kakinuma**

Abstract

A 3D real-space structural model for fuel cell catalysis systems, consisting of Pt and Gd-doped CeO₂ nanoparticles, was constructed to match simulated small angle X-ray scattering (SAXS) intensity and observed SAXS intensity using the reverse Monte–Carlo (RMC) method. The observed SAXS patterns were well reproduced by those of the simulations. The SAXS–RMC simulation results indicated that the number of nanometer-sized Pt particles is much smaller than the introduced amount. This suggests that most Pt particles are not uniformly distributed throughout the catalysts. Additionally, the coordination number of Pt particles, calculated from the structural model, tends to decrease as the amount of Pt loaded increases, which is consistent with the transmission electron microscopy (TEM) images. 3D pore size distributions using the obtained structure models were compared with the Barrett–Joyner–Halenda (BJH) analysis results for nitrogen gas adsorption data, and the lower quartiles and medians of the pore diameters were reasonably consistent. The presented SAXS–RMC modeling can evaluate both local arrangement of the constituent primary particles and aggregated mesoscale structure.

1. Introduction

Polymer electrolyte fuel cells (PEFC) are being actively researched due to their attractive properties such as high energy conversion efficiency, low operating temperature, light weight and compact size^{(1)–(6)}. A membrane electrode assembly (MEA) is the core device in a PEFC. The MEA consists of two porous electrodes, each comprising a catalyst layer and a gas diffusion layer, attached to both ends of a polymer electrolyte membrane. The typical material used for the catalyst layer is a Pt/C catalyst in which Pt nanoparticles are loaded on the carbon catalyst supports, but there is a well-known vulnerability to serious degradation during the startup and shutdown processes of the PEFC due to the oxygen reaction of the carbon catalyst supports in the cathode^{(7)–(15)}. Therefore, many studies have reported using electrically conductive ceramics as corrosion-resistant cathode catalyst supports^{(16)–(31)}. Recently, Shi *et al.* proposed superior oxygen reduction catalysis based on Pt nanoparticles supported by Gd-doped ceria (GDC)⁽³²⁾. The performance of the catalysis system is influenced by particle size distributions of both Pt and GDC, interconnected paths of the catalysis network, pore size distribution, and gas flow channels. For investigating such various structural features, it is necessary for characterizing from nanometer scale primary particles arrangement to several hundred nanometer scale aggregated structure. Recently, we suggested a 3D real-space modeling

approach for hierarchical materials by matching observed and simulated small angle X-ray scattering (SAXS) patterns using the reverse Monte–Carlo method^{(33), (34)} to construct a structural model of a silica aerogel, which is known as a mesoporous material⁽³⁵⁾. The 3D pore size distribution based on the obtained structural model was calculated using the spherical volume-weighted distance transformation (LTT: Local Thickness Transformation⁽³⁶⁾). The result was found to match well with the results of nitrogen gas adsorption experiments⁽³⁷⁾. Most recently, we applied this modeling to the Pt/GDC catalyst and compared the obtained structural model with the results of transmission electron microscopy (TEM) and nitrogen gas adsorption measurements⁽³⁸⁾. In this article, the details of our studies are introduced.

First, we will briefly explain our modified Debye scattering equation (mDSE), which is the main part of our modeling, and then explain how to apply it to the Pt/GDC catalysts system. Next, we will detail our nanoparticle packing structure modeling with the analysis procedures from building an initial structure model to estimating particle positions using the SAXS–RMC simulation. A comparison of the obtained results with those of the gas adsorption method and TEM is presented. Finally, the potential of the present non-destructive method for investigating complex 3D structures is discussed.

2. Scattering Intensity Calculation

2.1 Problem-solution approach

The X-ray scattering intensity in electron units of the scattering vector $\vec{q} = \vec{k}_{out} - \vec{k}_{in}$ (\vec{k}_{in} and \vec{k}_{out}) are

* X-ray Research Laboratory, Rigaku Corporation.

** Hydrogen and Fuel Cell Nanomaterials Center, University of Yamanashi.

the wavevectors of the incident and scattered X-rays, respectively) for a system composed of N individual particles is calculated from the following equation⁽³⁹⁾:

$$I(\vec{q}) = |F(\vec{q})|^2, \quad (1)$$

$$F(\vec{q}) = \sum_m^N f_m(q) \exp(i\vec{q} \cdot \vec{r}_m), \quad (2)$$

where $f_m(\vec{q})$ and \vec{r}_m are the form factors and positional vector of the m -th particles, respectively. The magnitude of the vector \vec{q} is expressed using the X-ray wavelength (λ) and the scattering angle (2θ) as $|\vec{q}| = 4\pi/\lambda \sin \theta$. If we assume an isotropic system and average the orientation of \vec{q} , then Equation (1) can be written as a function of $q = |\vec{q}|$,

$$I(q) = \sum_m^N \sum_n^N f_m(q) f_n(q) \text{sinc}(qr_{mn}), \quad (3)$$

where r_{mn} is the inter-particle distance ($r_{mn} = |\vec{r}_m - \vec{r}_n|$), and $\text{sinc}(x) = (\sin x)/x$. Equation (2) is the so-called ‘‘Debye scattering equation’’ (DSE)⁽⁴⁰⁾. The DSE is so well-known that a special issue of *Acta Crystallographica Section A* was published to celebrate its 100th anniversary⁽⁴¹⁾. The issue introduces an application of DSE transformation using a number density function when scatterers are atoms. It is possible to calculate the scattering intensity of a hierarchical structure from the DSE as long as we place the particles into real space. However, there are two main problems when applying the DSE to a large-scale structure model⁽⁴²⁾.

- ✓ 1. Low- q intensity profile oscillations: Oscillations in the low- q region caused by the finite box size effect can distort the scattering intensity profile.
- ✓ 2. Huge computational cost: the double summation required for all interparticle pair calculations results

in a computational cost that scales as $N^2 \propto L^6$, making it impractical for very large systems of box size L .

Previous approaches for addressing these problems are well known, as follows:

- ✓ First Problem Solution: Using a bigger simulation box to address oscillations in the low- q region caused by the finite box size effect.
 - ✓ Second Problem Solution: Introducing a number density function, $\rho(r)$, as shown in Appendix A, with a uniform form factor to mitigate the computational cost of L^6 for double summation in all interparticle pair calculations.
- However, these approaches do not fully solve the problems for the following reasons:
- ✓ Computational Capacity: Due to the L^6 computational cost, increasing L will exceed computational capacity.
 - ✓ Non-uniform Scattering Factors: Most materials do not have a significantly narrow particle size distribution to assume uniform scattering factors.

For these reasons, research on large-scale structures has not been adequately developed. We specifically demonstrate these problems using a structural model of silica aerogel⁽³¹⁾. As shown in Fig. 1, this structural model contains $N=117,846$ spherical particles arranged in a cubic simulation box with a size $L=300$ nm. The particle size is not uniform, as seen in the expanded view. Figure 2 shows the normalized (particle) number density function, $\rho(r)/\rho_0$. $\rho(r)$ is calculated by Equation (A3) in the appendix, where ρ_0 is the average number density, given by N/L^3 . The peak at $r=2.6$ nm corresponds to the first nearest neighbor distance. Since the volume, $\Delta V(r)$, used to calculate the number density is proportional to r^2 , the oscillations in $\rho(r)/\rho_0$ become smaller as r increases, and the value approaches $\rho(r)/\rho_0=1$ at long distance. The observed and calculated SAXS intensities based on the DSE and mDSE are shown in the upper part of Fig. 3. The scattering pattern of a

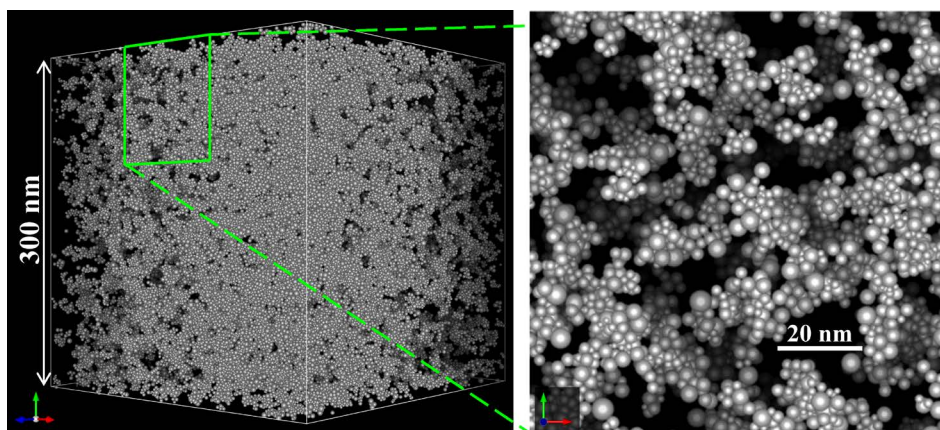


Fig. 1. Structural model of a silica aerogel estimated by a SAXS-RMC modeling⁽³⁵⁾. 117,846 spherical particles (volume fraction 5.6 vol%) are arranged in a cubic simulation box with side $L=300$ nm. The median pore size distribution of the model, 20 nm, is consistent with the results of nitrogen gas adsorption measurements⁽³⁷⁾.

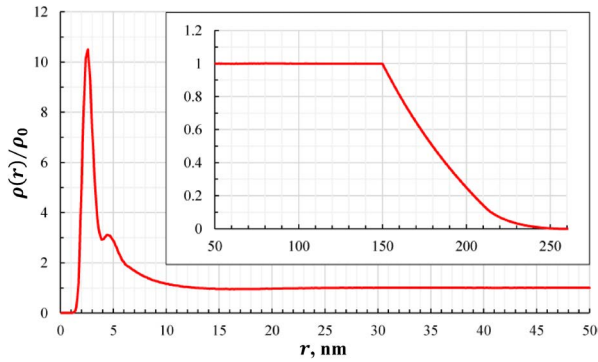


Fig. 2. Normalized number density function $\rho(r)/\rho_0$ of silica aerogel particles. The horizontal axis r is the interparticle distance. The decrease of $\rho(r)/\rho_0$ in the $r \geq 150$ nm ($=L/2$) regime is caused by the finite box size effect.

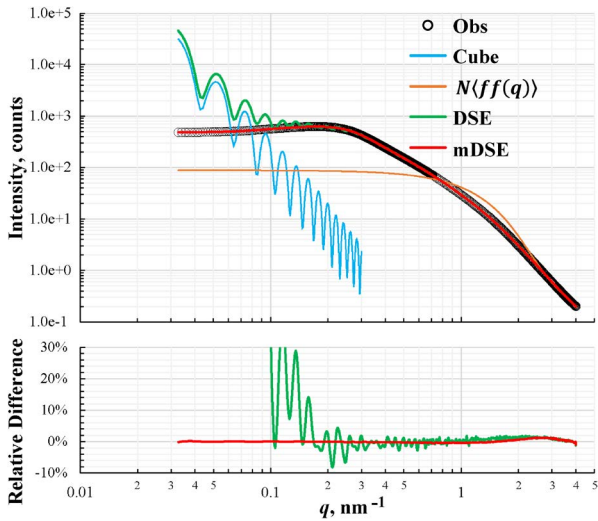


Fig. 3. Comparison of SAXS patterns. The upper pattern is the scattering intensity. The lower pattern is the relative difference $\Delta I(q)/I_{\text{obs}}(q) = \{I_{\text{calc}}(q) - I_{\text{obs}}(q)\}/I_{\text{obs}}(q)$. Obs is the observed intensity (open circles), Cube is that of a cube particle with a 300 nm size (blue line), $\langle ff(q) \rangle$ is that of average scattering factors (orange line), DSE (green line), mDSE (red line). The Cube intensity was calculated using a superbball^{(43), (44)} model in the software SasView Ver.5.0.5 (<https://www.sasview.org/>).

cube with the length of one side equal to 300 nm and average scattering factors $\langle ff(q) \rangle = \{\sum_i^N \sum_j^N f_i(q) f_j(q)\}/N^2$ of the isolated particles are also shown. The lower part of Fig. 3 shows the relative differences, $\Delta I(q)/I_{\text{obs}}(q)$ as described in Appendix B, for DSE and mDSE calculations. In the former, significant oscillations appear in the low- q region of $q < 0.2 \text{ nm}^{-1}$. This is the first problem identified above, and the period of oscillation matches that of the cube. It is caused by the finite size effect of the simulation box as shown in the inset of Fig. 2. To overcome the problem, we devised a simple solution that divides the DSE into three terms

based on the correlation distance:

- ✓ First term (short-distance correlations): Using individual form factors $f_i(q)f_j(q)$.
- ✓ Second term (long-distance correlations): Using the number density function $\rho(r)$ to minimize the L^6 cost.
- ✓ Third term (distance longer than half the simulation box size): Using the average density $\langle \rho \rangle$ to solve the first problem.

Introducing these modifications, taking the instrumental resolution function into consideration, can be expressed as the following modified Debye scattering equation (mDSE):

$$I(q) = \sum_i^N \sum_{j \in r_{ij} \leq R}^N f_i(q) f_j(q) H(q, r_{ij}) + 4\pi N \langle ff(q) \rangle \int_R^{\frac{L}{2}} r^2 \rho(r) H(q, r) dr + 4\pi N \langle ff(q) \rangle \langle \rho \rangle \int_{\frac{L}{2}}^{\infty} r^2 H(q, r) dr, \quad (4)$$

where

$$H(q, r) = \text{sinc}(qr) \exp\left(-\frac{\Delta q^2 r^2}{2}\right), \quad (5)$$

and R is a switching distance between the first and second terms. It is assumed that when the interparticle distance $r > R$, the individual scattering factors $f_i(q) f_j(q)$ can be replaced by the mean value $\langle ff(q) \rangle$. We also take into account the resolution of a real X-ray instrument used for the measurements, Δq , which is determined by the incident beam divergence and the resolution of the detecting system⁽³⁵⁾. The key to performing highly accurate calculations using the mDSE is that the number of particles $\Delta V(R)\rho(R)$ contained in the integral volume $\Delta V(R)$ is statistically large enough to allow individual scattering factors to be replaced by the mean value $\langle ff(q) \rangle$. The value of R that satisfies this condition is related to the particle size and the magnitude of their statistical dispersion. If the particle size and/or its dispersion are small, a smaller R value can be applied to the mDSE, resulting in a smaller computational cost.

2.2 Extend to multiple types of particles series

To analyze catalysis systems, we need to extend the previous formulation to treat multiconstituent systems by introducing M different types of primary particle series as follows:

$$I(q) = \sum_a^M \sum_b^M I_{a\beta}(q) + 4\pi N \langle ff(q) \rangle \langle \rho \rangle \int_{\frac{L}{2}}^{\infty} r^2 H(q, r) dr, \quad (6)$$

$$\begin{aligned}
 I_{\alpha\beta}(q) = & \sum_{i_{\alpha}}^{N_{\alpha}} \sum_{j_{\beta} \in r_{i_{\alpha}j_{\beta}} \leq R_{\alpha\beta}}^{N_{\beta}} f_{i_{\alpha}}(q) f_{j_{\beta}}(q) H(q, r_{i_{\alpha}j_{\beta}}) \\
 & + 4\pi \sqrt{N_{\alpha} N_{\beta}} \langle f_{\alpha} f_{\beta}(q) \rangle \\
 & \times \int_{R_{\alpha\beta}}^{\frac{L}{2}} r^2 \rho_{\alpha\beta}(r) H(q, r) dr, \quad (7)
 \end{aligned}$$

where, N_{α} and N_{β} are the total numbers of type α and β particle series, respectively, in the simulation box. i_{α} means the i -th particle in the α type particle series. $\langle f_{\alpha} f_{\beta}(q) \rangle = 1/N_{\alpha} N_{\beta} \sum_{i_{\alpha}}^{N_{\alpha}} \sum_{j_{\beta}}^{N_{\beta}} f_{i_{\alpha}}(q) f_{j_{\beta}}(q)$. $\rho_{\alpha\beta}(r)$ is a local number density of type β particles relative to type α particles. When $r > L/2$, the number density $\rho_{\alpha\beta}(r)$ is assumed to be the constant value $\sqrt{N_{\alpha} N_{\beta}}/L^3$. To reduce the computational cost, we introduce a switching distance $R_{\alpha\beta}$ for each combination of particle series.

When the catalyst particle series is C and the support particle series is S , they are introduced into Equation (6) as follows:

$$\begin{aligned}
 I(q) = & I_{CC}(q) + I_{SS}(q) + 2I_{CS}(q) \\
 & + 4\pi N \langle ff(q) \rangle \langle \rho \rangle \int_{\frac{L}{2}}^{\infty} r^2 H(q, r) dr. \quad (8)
 \end{aligned}$$

In most catalysts, including this Pt/GDC catalyst, the particle size of the catalysts is much smaller than that of the supports. Therefore, using a smaller R_{CC} can minimize the computational cost in the $I_{CC}(q)$ calculation.

3. Synthesis and Characterization

3.1 Synthesis of catalyst powder

The synthesis of GDC supports and the loading of Pt catalysts were carried out by the flame oxide-synthesis method and colloid method⁽¹⁸⁾, respectively. For detailed procedures, please refer to the paper by Shi *et al.*⁽³²⁾ The projected Pt loading on GDC supports were 0, 20, 40, and 50 wt%. To indicate the Pt loading values, the samples were termed S-0, S-20, S-40, and S-50.

3.2 Characterization

The pore size distribution was derived from a nitrogen gas adsorption measurement (Autosorb-iQ, Anton-Paar GmbH, Austria) using the Barrett–Joyner–Halenda (BJH) method⁽⁴⁵⁾. The Pt content in the resultant catalyst was quantified by inductively coupled plasma-mass spectrometry (ICP-MS, 7500CX, Agilent Technologies Co. Ltd., USA). TEM images of the synthesized catalyst were taken using a H-9500 microscope (Hitachi High-Tech. Co., Japan). SAXS measurements were performed using a laboratory SAXS measurement system (Rigaku NANOPIX), which employs a high-performance semiconductor detector (Rigaku HyPix-6000), a high-brilliance point-focus X-ray source (Rigaku MicroMax-007 HFMR) focused

by a multilayer confocal mirror (Rigaku OptiSAXS), and combinations of low parasitic scattering pinhole slits (Rigaku ClearPinhole).

The SAXS patterns for samples S-0, S-20, S-40, and S-50 were collected in transmission geometry. The q space resolution of the instrument under the current measurement conditions was $\Delta q = 0.0067 \text{ nm}^{-1}$. This resolution was used for the construction of 3D structural models based on the mDSE to fit the experimental SAXS profiles. The procedure for structural model analysis is explained in the next section. Local thickness transformation (LTT)^{(36), (37)} was used as the analysis algorithm for the 3D pore size distribution of the structural model. The 3D structural model and pore size distribution were visualized using the software VESTA3⁽⁴⁶⁾.

4. Simulation Procedure and Results

We have introduced two primary particle series, Pt catalyst and GDC support, to build the Pt/GDC catalyst structure model. To build an initial structural model, it is necessary to determine the size distributions $pdf_{\alpha}(x)$ of the particles. A $pdf_{\text{GDC}}(x)$ for GDC particles was determined by matching the observed S-0 pattern in the high- q regime ($0.6 < q < 2 \text{ nm}^{-1}$), as shown in Fig. 4. The obtained average diameter \bar{d}_{GDC} and the coefficient of variation CV_{GDC} of the particles were 11.86 nm and 0.305, respectively, assuming $pdf_{\text{GDC}}(x)$ follows a log-normal distribution. To determine the $pdf_{\text{Pt}}(x)$ for Pt particles, we used TEM images at selected points to extract Pt particles, as shown in Fig. 5, and fitted with log-normal distribution. The obtained average diameter \bar{d}_{Pt} and coefficient of variation CV_{Pt} are listed in Table 1. It should be noted that the selected points of the TEM images were chosen from locations where the specimens were thin enough to easily identify either Pt or GDC particles, and they may not be representative of the whole structure. The weight ratio of the Pt catalyst w_{Pt} was determined by inductively coupled plasma-atomic emission spectroscopy (ICP-AES) analysis, and the

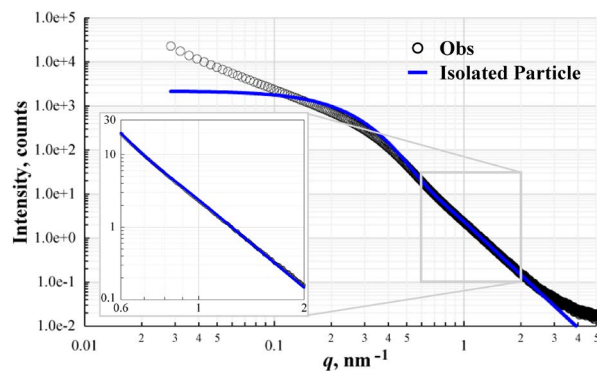


Fig. 4. Estimation of the size distribution analysis of GDC particles by comparing the scattering intensity of the isolated-particle simulation and observed S-0 data in the q regime from 0.6 to 2 nm^{-1} . Reference: K. Omote *et al.*, *Adv. Theory Simul.*, (2023), 2300713. <https://doi.org/10.1002/adts.202300713>

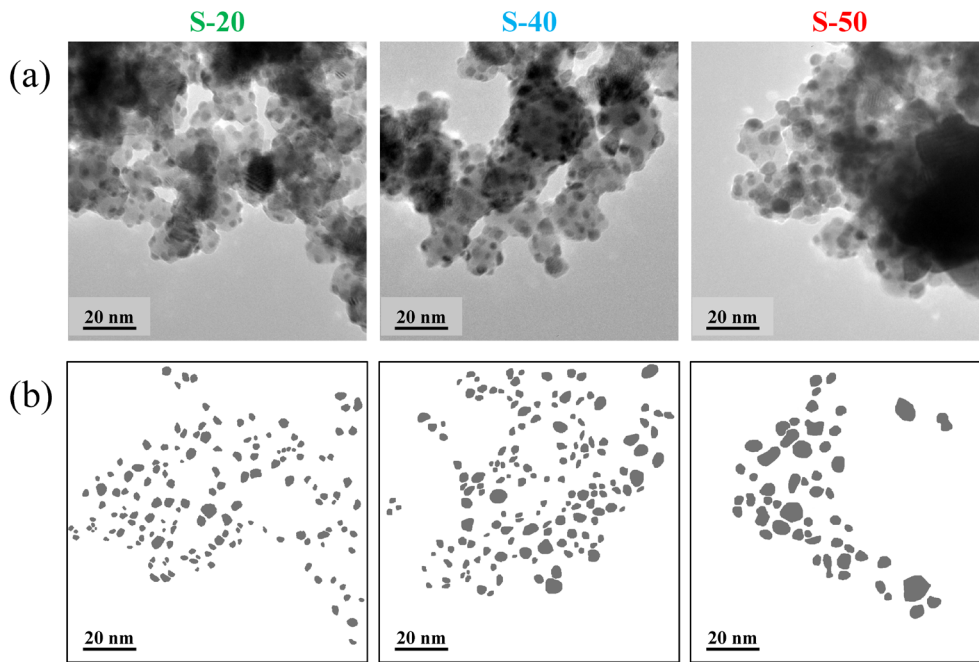


Fig. 5. A typical TEM image (a) with the selected points to measure Pt particle size (b). Reference: K. Omote *et al.*, *Adv. Theory Simul.*, (2023), 2300713. <https://doi.org/10.1002/adts.202300713>

Table 1. Structural properties of catalyst powders. Reference: K. Omote *et al.*, *Adv. Theory Simul.*, (2023), 2300713. <https://doi.org/10.1002/adts.202300713>

	S-0	S-20	S-40	S-50
\bar{d}_{Pt} , CV _{Pt} ^{a)}		1.75 nm, 0.349	2.28 nm, 0.348	3.10 nm, 0.267
w_{Pt} ^{b)} (wt%)		19.6	39.0	53.6
v_{pore} ^{c)} (cm ³ /g)	1.539	0.454	0.377	0.249

a) Size distribution parameters, the average diameter \bar{d}_{Pt} and the coefficient of variation CV_{Pt}, of Pt particles were determined from TEM images.

b) Weight ratio of Pt particles w_{Pt} was determined by ICP-AES analysis.

c) Total volume of pores v_{pore} was directly calculated from the volume of adsorbed nitrogen gas at the highest relative pressure.

total pore volume v_{pore} was directly calculated from the volume of adsorbed nitrogen gas at the highest relative pressure. The results are also listed in Table 1.

Volume percentages of Pt particles V_{Pt} and GDC particles V_{GDC} , and pores V_{pore} were estimated using the following equations:

$$\begin{cases} v_{\text{Pt}} : v_{\text{GDC}} : v_{\text{pore}} = V_{\text{Pt}} : V_{\text{GDC}} : V_{\text{pore}}, \\ V_{\text{Pt}} + V_{\text{GDC}} + V_{\text{pore}} = 100 \text{ vol}\%, \\ w_{\text{Pt}} : 1 - w_{\text{Pt}} = \rho_{\text{Pt}} v_{\text{Pt}} : \rho_{\text{GDC}} v_{\text{GDC}} \end{cases} \quad (9)$$

where v_{Pt} and v_{GDC} are the volumes of Pt and GDC particles, respectively, in 1 g of the sample. ρ_{Pt} and ρ_{GDC} are the crystal densities of the Pt catalysts and GDC supports, respectively. Substituting the literature values, $\rho_{\text{Pt}} = 21.43 \text{ g cm}^{-3}$ (Inorganic crystal structure database (ICSD) code: 180980) and $\rho_{\text{GDC}} = 7.25 \text{ g cm}^{-3}$ (ICSD code: 28796), the volume percentages of Pt, GDC, and pore ($V_{\text{Pt}} : V_{\text{GDC}} : V_{\text{pore}}$) are calculated as follows: S-0: (0 : 8.2 : 91.8), S-20: (1.6 : 19.3 : 79.1), S-40: (3.9 : 17.3 : 78.8), and S-50: (7.4 : 18.9 : 73.7).

For the SAXS-RMC simulation study, we filled GDC and Pt particles into a 400 nm simulation box based on the above estimated numbers. The resultant total number of GDC particles was 4,852, 11,142, 10,084 and 10,961 for S-0, S-20, S-40, and S-50, respectively. From the above-estimated values V_{Pt} , the total number of Pt particles was calculated as 264,067, 291,161, and 249,957, for S-20, S-40, and S-50, respectively. The initial positions of the GDC particles were selected by sets of uniform random numbers (x , y , z). The Pt particles were assumed to touch the surface of the randomly selected GDC particles. An additional assumption was made to avoid overlapping particles during the subsequent SAXS-RMC simulation.

We adopted a goodness-of-fit between the simulation and the observed data to optimize the constructed structure using the weight function (w_i) as follows⁽³⁵⁾:

$$\begin{cases} w_{i>0} \equiv \ln q_{i-1} - \ln q_i \\ w_0 = w_1, \end{cases} \quad (10)$$

$$\chi^2 = \frac{\sum_i w_i [\ln I_{\text{obs}}(q_i) - \ln I_{\text{calc}}(q_i)]^2}{\sum_i w_i [\ln I_{\text{obs}}(q_i)]^2}, \quad (11)$$

where, i is the i -th measurement data point. For the conditions in Equation (8), the switching distances R_{CC} for Pt–Pt pair calculation, R_{SS} for GDC–GDC pair, and R_{CS} for Pt–GDC pair are 50, 200, and 200 nm, respectively. The differences in the scattering intensities between $R_{CC}=50$ nm and $R_{CC}=200$ nm were confirmed to be less than $\pm 3\%$ for all samples, which significantly saved computational time.

Each RMC iteration proceeds as follows;

- ✓ First step: Randomly select particles and modify their positions.
- ✓ Second step: Evaluate the goodness-of-fit, χ_{New} , after the positional modification.
- ✓ Third step: Compare this value with the value before the positional modification, χ_{Current} . If $\chi_{\text{New}} < \chi_{\text{Current}}$, then the model including the modified positions is accepted.

Since Shi *et al.* have reported that all of the GDC particles were connected due to partial sintering and necking formation with nearest neighbor particles to form a network microstructure⁽³²⁾, we adopted an additional assumption: when modifying a GDC particle's position, it must touch the surface of a randomly selected GDC particle. Observed and simulated scattering intensities with their relative differences are shown in Fig. 6. However, there was a large mismatch between the observed and simulated patterns for S-20, S-40, and S-50. Specifically, the simulated intensities were higher than the observed intensities in the $q > 1 \text{ nm}^{-1}$ regime, where Pt particle

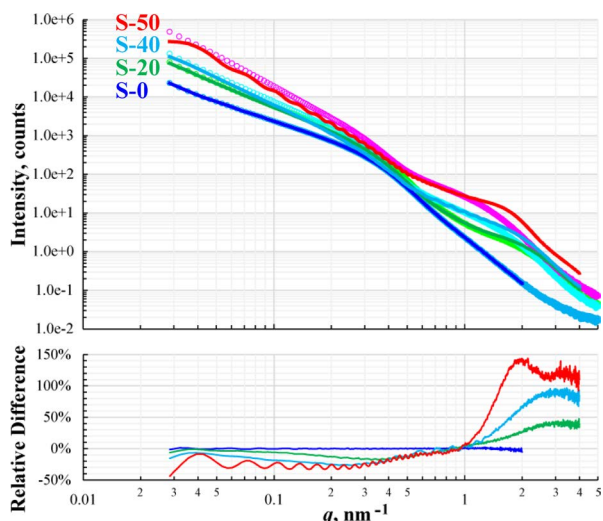


Fig. 6. Observed scattering intensity (upper open circles) and simulated patterns (solid lines) before optimizing the Pt volume fraction. The simulated patterns with introduced Pt contents do not match the observed patterns. Reference: K. Omote *et al.*, *Adv. Theory Simul.*, (2023), 2300713. <https://doi.org/10.1002/adts.202300713>

contribution is dominant. This suggests that the number of Pt particles should be adjusted, as shown in Fig. 7, to find the optimum number of Pt particles. The results show that χ displayed a clear minimum value at a certain number of Pt particles for all samples. By using the Pt volume fractions that give minimum χ values, the simulated SAXS patterns are in good agreement with the observed patterns over the entire q regime. However, we noticed that the resultant best-fit volume fractions of Pt particles are significantly lower than the original values: 1.6 to 0.8 vol%, 3.9 to 1.0 vol%, and 7.4 to 0.8 vol%, for S-20, S-40, and S-50, respectively. This result suggests that most of the introduced Pt particles are not uniformly distributed throughout the whole catalyst system, especially in cases with higher volume fractions. It is emphasized that the SAXS pattern can provide information concerning the ratio of the volume fraction of smaller and larger particle sizes if the size difference is sufficient, as seen in the current Pt/GDC catalyst system. Consequently, we infer that the derived structural features from TEM images using selected locations, where the specimens were thin enough to easily identify either Pt or GDC particles, may not be representative of the entire structure.

The constructed 3D structures obtained from the present SAXS-RMC modeling are shown in Fig. 8. To characterize these 3D structures, the coordination number distribution histogram, $Y_{SC}(X)$, is shown in Fig. 9. This histogram is obtained using Equation (C3) in the appendix, where the GDC is the central particle and the Pt is the neighboring particle. We used the value $\epsilon=0.01$ in this calculation. The mean values of coordination number, $\overline{X}_{SC} = \sum_{X=0}^{\infty} X Y_{SC}(X)$, are 12.8, 3.5, and 2.0, for S-20, S-40, and S-50, respectively, clearly indicating a decreasing coordination number with increasing introduced Pt amount. In particular, for S-40 and S-50, we observed that a significant number of GDC particles have no neighboring Pt particles ($X=0$), as illustrated in Fig. 9. This suggests that as the Pt content increases, more GDC particles remain uncoordinated with Pt particles. It should be emphasized that the SAXS-RMC modeling enables the analysis of such statistical features in the whole sample area. It is a complementary technique for TEM, which is suited for analyzing nanometer scale local structure.

One of the key statistical features of the catalyst can be expressed by the pore size distribution. The actual LTT^{(36), (37)} are performed at $200 \times 200 \times 200$ grid points on the structural model in Fig. 8, and the obtained 3D pore size distribution (in color map style) are shown in Fig. 10. It must be noted that the obtained model is only one plausible structures that matches the observed SAXS pattern, because there is a huge number of constituent particles the exact positions of all of them cannot be determined. To confirm the uniqueness of the extracted statistical features, we tried RMC runs starting from three independent initial random structures, and almost the same structural features were obtained. The cumulative pore volume $C(d)$, obtained

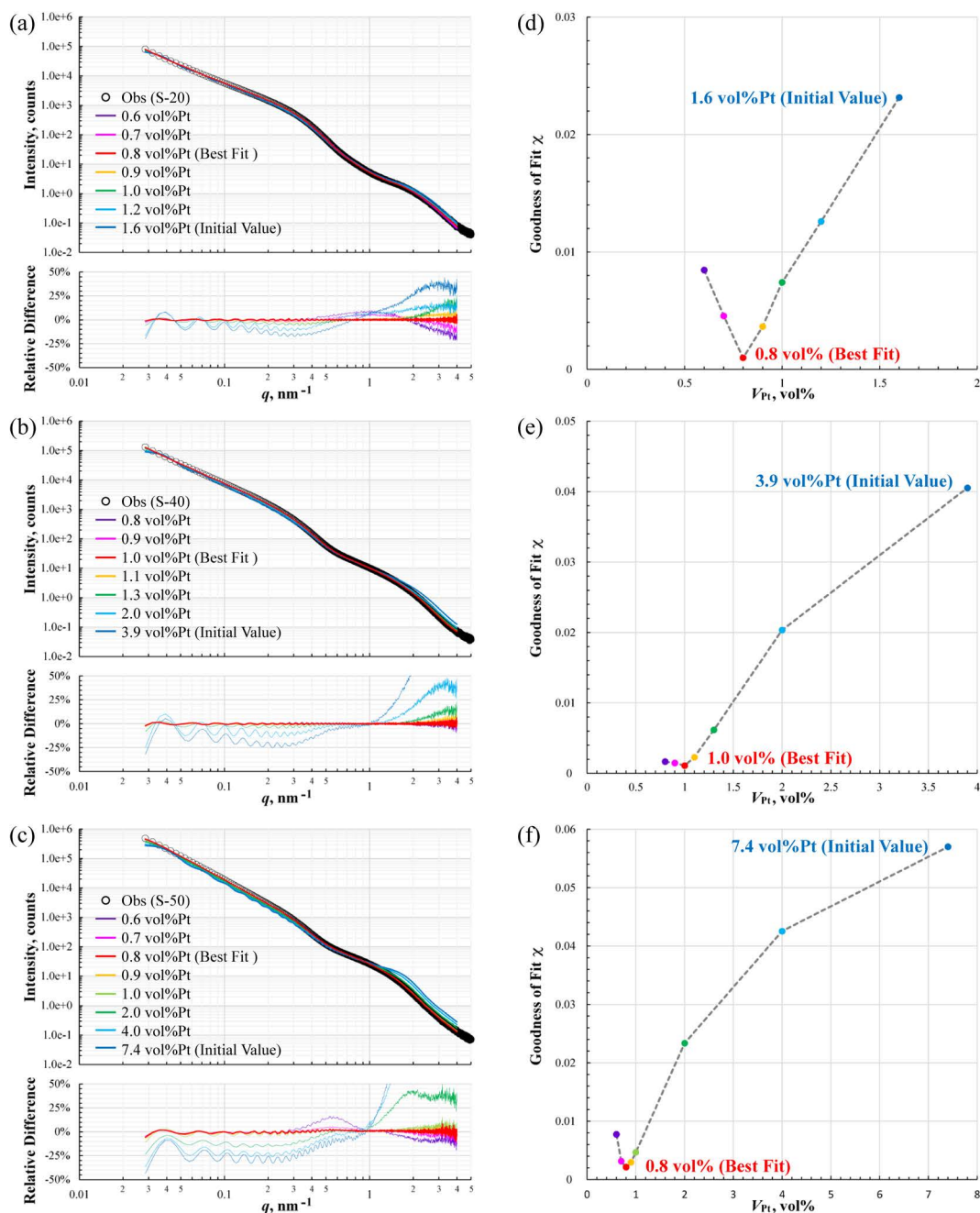


Fig. 7. Optimization for Pt particle contents by varying Pt vol%. Observed scattering intensity (black open circles) and simulated patterns (solid lines) are shown in (a), (b), and (c) for S-20, S-40, and S-50, respectively. The χ values versus V_{Pt} are shown in (d), (e), and (f) for S-20, S-40, and S-50, respectively. Reference: K. Omote *et al.*, *Adv. Theory Simul.*, (2023), 2300713. <https://doi.org/10.1002/adts.202300713>

by SAXS and BJH methods, with the horizontal axis representing pore diameter d , is shown in Fig. 11. The statistical values (mean D_{ave} and the quartiles Q_n) are listed in Table 2. Because the measurement steps of the nitrogen gas adsorption were not small enough, a linear interpolated curve for $C(d)$ was used to calculate the Q_n values. We infer that the static values of the BJH analysis results are unreliable because of the large influence of a few measurement points in the higher d regime with large volume changes. In particular, the result for S-0 shows relatively large volume changes ($C(162) - C(54.6) = 91.8 - 8.7 = 83.1$ vol%) at the last two

measurement points, which are 54.6 to 162 nm in d . Even considering this uncertainty in the BJH results, the obtained lower quartile Q_1 and median Q_2 are reasonably consistent with each other, except for the result of S-0. This may be because S-0 has a relatively large pore size in the BJH results, so the observed minimum value of q in SAXS data may not be small enough.

5. Conclusions

We have developed a SAXS-RMC modeling method applicable to multiconstituent systems for studying

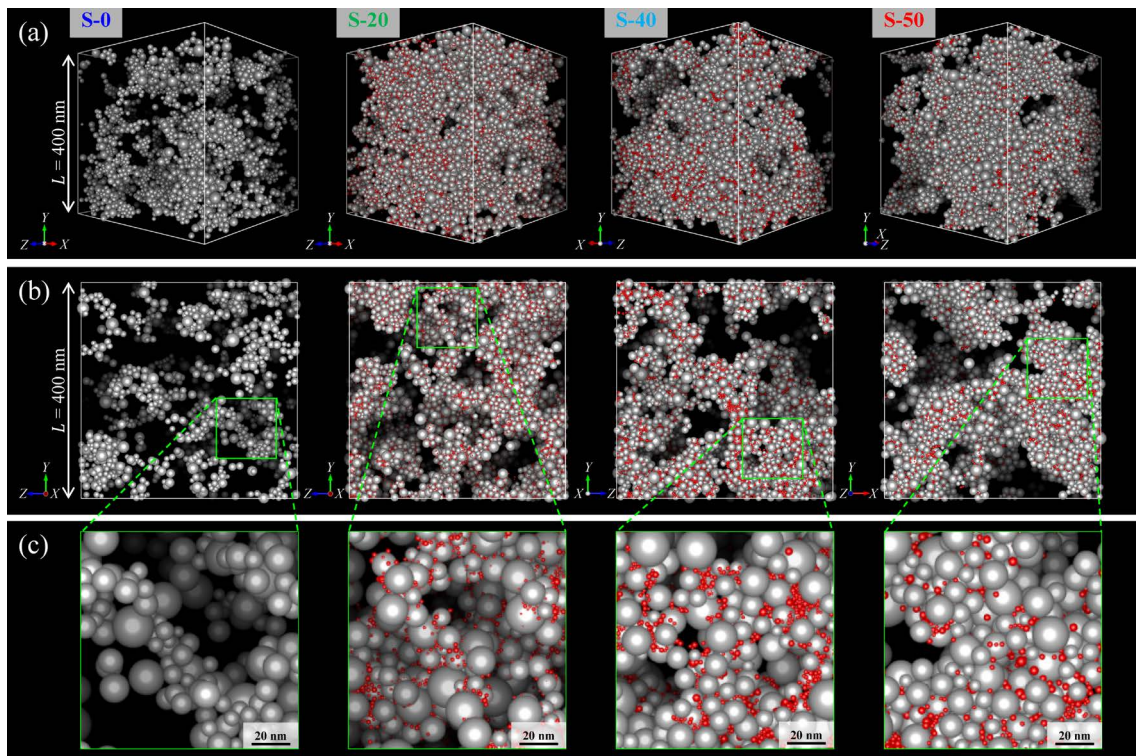


Fig. 8. The resultant structural models obtained by RMC to match the observed SAXS patterns. Red and gray spheres for Pt and GDC particles, respectively. a) 3D structural models in the perspective projection. b) The models in the parallel projection. c) Magnified images of (b).

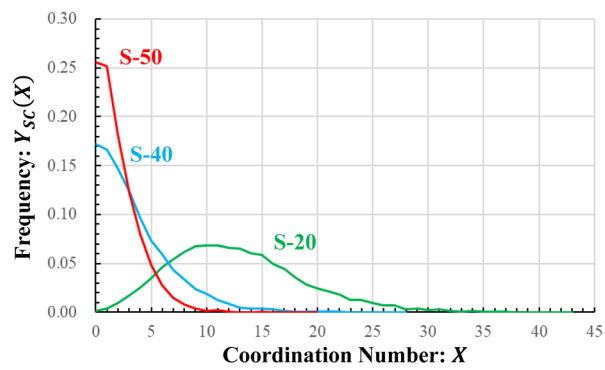


Fig. 9. Histogram of Pt-particle coordination number on GDC particle. No Pt coordinated GDC particles $Y_{sc}(0) \neq 0$ exist for S-40 and S-50. Reference: K. Omote *et al.*, *Adv. Theory Simul.*, (2023), 2300713. <https://doi.org/10.1002/adts.202300713>

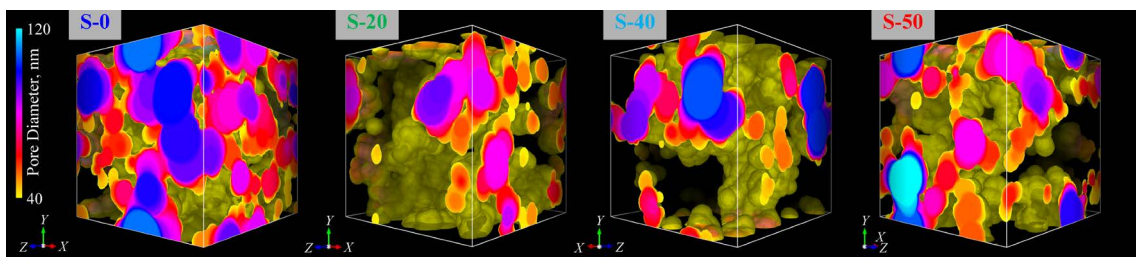


Fig. 10. 3D pore size distributions represented by color maps with a yellow isosurface level of 40 nm in diameter.

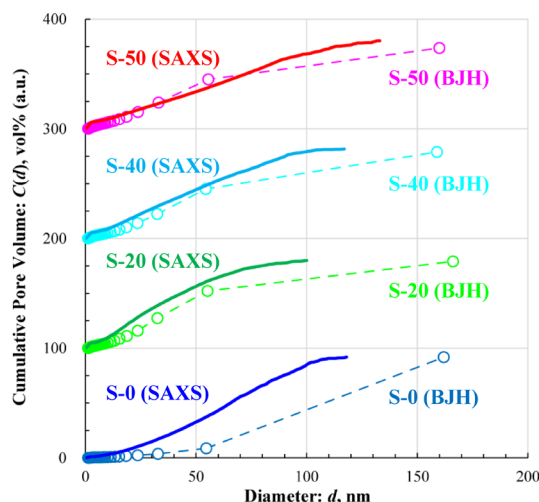


Fig. 11. Pore size distribution curves. The BJH analysis result curves are shown in the dashed lines with the measurement data points in open circles. The average curves of three RMC simulations run for SAXS patterns are shown in the solid lines. The maximum values $C(d_{max})$ of BJH and SAXS are V_{pore} and $1 - 1/L^3 \sum_i^N 4\pi/3(R_i)^3$, respectively, where R_i is i -th particle radius. Reference: K. Omote *et al.*, *Adv. Theory Simul.*, (2023), 2300713. <https://doi.org/10.1002/adts.202300713>

Table 2. Means D_{ave} (nm) and the quartiles Q_n (nm) of the pore size distribution. Reference: K. Omote *et al.*, *Adv. Theory Simul.*, (2023), 2300713. <https://doi.org/10.1002/adts.202300713>

	S-0	S-20	S-40	S-50
$D_{ave}^{BJH}/D_{ave}^{SAXS}$ (Means)	95 / 61	63 / 37	68 / 47	66 / 58
Q_1^{BJH}/Q_1^{SAXS} (Lower quartiles)	73 / 40	27 / 18	30 / 23	27 / 28
Q_2^{BJH}/Q_2^{SAXS} (Medians)	103 / 62	44 / 34	49 / 45	47 / 59
Q_3^{BJH}/Q_3^{SAXS} (Upper quartiles)	132 / 83	84 / 54	98 / 72	93 / 85

the 3D packing structure of Pt/GDC catalysts and successfully constructed 3D models that match the observed SAXS patterns. We found that the observed SAXS patterns are sensitive to the ratio of the number of particles between GDC and Pt. By performing SAXS-RMC simulations with varying numbers of Pt particles, we identified clear optimum numbers. The results suggest that the uniformly distributed Pt particles are significantly fewer than the introduced amount, allowing us to estimate the Pt particle coordination number on the GDC support.

Pore size distributions of the obtained 3D structural models were compared with the BJH analysis of nitrogen gas adsorption data, and the lower quartiles and medians of pore diameters were reasonably consistent with each other. It could be interesting to evaluate physical properties such as gas diffusivity, electric conductivity, and so on, based on the constructed structural model of those complex systems.

Acknowledgment

Part of this study is based on results obtained from a project commissioned by the New Energy and Industrial Technology Development Organization (NEDO).

References

(1) R. K. Ahluwalia and X. Wang: *J. Power Sources*, **177** (2008),

- 167–176. <https://doi.org/10.1016/j.jpowsour.2007.10.026>
- (2) M. Uchida, Y.-C. Park, K. Kakinuma, H. Yano, D. A. Tryk, T. Kamino, H. Uchida and M. Watanabe: *Phys. Chem. Chem. Phys.*, **15** (2013), 11236–11247. <https://doi.org/10.1039/C3CP51801A>
- (3) Y.-C. Park, K. Kakinuma, H. Uchida, M. Watanabe and M. Uchida: *J. Power Sources*, **275** (2015), 384–391. <https://doi.org/10.1016/j.jpowsour.2014.10.149>
- (4) Y.-C. Park, H. Tokiwa, K. Kakinuma, M. Watanabe and M. Uchida: *J. Power Sources*, **315** (2016), 179–191. <https://doi.org/10.1016/j.jpowsour.2016.02.091>
- (5) R. Shimizu, Y.-C. Park, K. Kakinuma, A. Iiyama and M. Uchida: *J. Electrochem. Soc.*, **165** (2018), F3063–F3071. <http://doi.org/10.1149/2.0071806jes>
- (6) M. Uchida: *Current Opinion in Electrochemistry*, **21** (2020), 209–218. <https://doi.org/10.1016/j.coelec.2020.02.019>
- (7) D. A. Stevens, M. T. Hicks, G. M. Haugen and J. R. Dahn: *J. Electrochem. Soc.*, **152** (2005) A2309–A2315. <https://doi.org/10.1149/1.2097361>
- (8) C. A. Reiser, L. Bregoli, T. W. Patterson, J. S. Yi, J. Deliang, M. L. Perry and T. D. Jarvi: *Electrochem. Solid-State Lett.*, **8** (2005) A273–A276. <https://doi.org/10.1149/1.1896466>
- (9) L. M. Roen, C. H. Paik and T. D. Jarvi: *Electrochem. Solid-State Lett.*, **7** (2004) A19–A22. <https://doi.org/10.1149/1.1630412>
- (10) K. H. Kangasniemi, D. A. Condit and T. D. Jarvi: *J. Electrochem. Soc.*, **151** (2004) E125–E132. <https://doi.org/10.1149/1.1649756>
- (11) J. P. Meyers and R. M. Darling: *J. Electrochem. Soc.*, **153** (2006) A1432–A1443. <https://doi.org/10.1149/1.2203811>
- (12) M. Lee, M. Uchida, K. Okaya, H. Uchida and M. Watanabe: *Electrochemistry*, **79** (2011), 381–387.
- (13) M. Hara, M. Lee, C.-H. Liu, B.-H. Chen, Y. Yamashita, M. Uchida, H. Uchida and M. Watanabe: *Electrochim. Acta*, **70** (2012), 171–181. <https://doi.org/10.1016/j.electacta.2012.03.043>
- (14) Y.-C. Park, K. Kakinuma, M. Uchida, D. A. Tryk, T. Kamino,

- H. Uchida and M. Watanabe: *Electrochim. Acta*, **91** (2013), 195–207. <https://doi.org/10.1016/j.electacta.2012.12.082>
- (15) Y. Yamashita, S. Itami, J. Takano, K. Kakinuma, H. Uchida, M. Watanabe, A. Iiyama and M. Uchida: *J. Electrochem. Soc.*, **164** (2017), F181–F187. <https://doi.org/10.1149/2.0101704jes>
- (16) A. Masao, S. Noda, F. Takasaki, K. Ito and K. Sasaki: *Electrochem. Solid-State Lett.*, **12** (2009), B119–B122. <https://doi.org/10.1149/1.3152325>
- (17) K. Kakinuma, M. Uchida, T. Kamino, H. Uchida and M. Watanabe: *Electrochim. Acta*, **56** (2011), 2881–2887. <https://doi.org/10.1016/j.electacta.2010.12.077>
- (18) K. Kakinuma, Y. Chino, Y. Senoo, M. Uchida, T. Kamino, H. Uchida, S. Deki and M. Watanabe: *Electrochim. Acta*, **110** (2013), 316–324. <https://doi.org/10.1016/j.electacta.2013.06.127>
- (19) Y. Senoo, K. Kakinuma, M. Uchida, H. Uchida, S. Deki and M. Watanabe: *RSC Adv.*, **4** (2014), 32180–32188. <https://doi.org/10.1039/c4ra03988b>
- (20) E. Fabbri, A. Rabis, R. Kötz and T. J. Schmidt: *Phys. Chem. Chem. Phys.*, **16** (2014), 13672–13681. <https://doi.org/10.1039/c4cp00238e>
- (21) Y. Senoo, K. Taniguchi, K. Kakinuma, M. Uchida, H. Uchida, S. Deki and M. Watanabe: *Electrochem. Commun.*, **51** (2015), 37–40. <https://doi.org/10.1016/j.elecom.2014.12.005>
- (22) Y. Chino, K. Kakinuma, D. A. Tryk, M. Watanabe and M. Uchida: *J. Electrochem. Soc.*, **163** (2015), F97–F105. <https://doi.org/10.1149/2.0571602jes>
- (23) K. Takahashi, R. Koda, K. Kakinuma and M. Uchida: *J. Electrochem. Soc.*, **164** (2017), F235–F242. <https://doi.org/10.1149/2.0251704jes>
- (24) K. Kakinuma, N. Hirayama, A. Iiyama, M. Watanabe and M. Uchida: *J. Electrochem. Soc.*, **164** (2017), F1226–F1233. <https://doi.org/10.1149/2.1461712jes>
- (25) C. Takei, R. Kobayashi, Y. Mizushita, Y. Hiramitsu, K. Kakinuma and M. Uchida: *J. Electrochem. Soc.*, **165** (2018), F1300–F1311. <https://doi.org/10.1149/2.0591816jes>
- (26) K. Kakinuma, R. Kobayashi, A. Iiyama and M. Uchida: *J. Electrochem. Soc.*, **165** (2018), J3083–J3089. <https://doi.org/10.1149/2.0141815jes>
- (27) H. Ohno, S. Nohara, K. Kakinuma, M. Uchida and H. Uchida: *Catalysts*, **9**(1) (2019), 74. <https://doi.org/10.3390/catal9010074>
- (28) K. Kakinuma, K. Suda, R. Kobayashi, T. Tano, C. Arata, I. Amemiya, S. Watanabe, M. Matsumoto, H. Imai, A. Iiyama and M. Uchida: *ACS Appl. Mater. Interfaces*, **11**, **38** (2019), 34957–34963. <https://doi.org/10.1021/acsami.9b11119>
- (29) K. Kakinuma, M. Hayashi, T. Hashimoto, A. Iiyama and M. Uchida: *ACS Appl. Energy Mater.*, **3**, **7** (2020), 6922–6928. <https://doi.org/10.1021/acsaem.0c00993>
- (30) G. Shi, T. Tano, D. A. Tryk, A. Iiyama, M. Uchida and K. Kakinuma: *ACS Catal.*, **11** (2021), 5222–5230. <https://doi.org/10.1021/acscatal.0c05157>
- (31) G. Shi, T. Hashimoto, D. A. Tryk, T. Tano, A. Iiyama, M. Uchida and K. Kakinuma: *Electrochim. Acta*, **390** (2021), 138894. <https://doi.org/10.1016/j.electacta.2021.138894>
- (32) G. Shi, T. Tano, D. A. Tryk, A. Iiyama, M. Uchida, Y. Kuwauchi, A. Masuda and K. Kakinuma: *J. Catal.*, **407** (2022), 300–311. <https://doi.org/10.1016/j.jcat.2022.02.009>
- (33) R. L. McGreevy and L. Pusztai: *Mol. Simul.*, **1** (1988), 359–367. <https://doi.org/10.1080/08927028808080958>
- (34) D. A. Keen and R. L. McGreevy: *Nature*, **344** (1990), 423–425. <https://doi.org/10.1038/344423a0>
- (35) K. Omote and T. Iwata: *J. Appl. Cryst.*, **54** (2021), 1290–1297. <https://doi.org/10.1107/S1600576721006701>
- (36) T. Hildebrand and P. Rüesgsegger: *J. Microsc.*, **185** (1997), 67–75. <https://doi.org/10.1046/j.1365-2818.1997.1340694.x>
- (37) T. Iwata: *Rigaku Journal*, **38** (2022), No. 2, 7–14.
- (38) K. Omote, T. Iwata and K. Kakinuma: *Adv. Theory Simul.*, (2023), 2300713. <https://doi.org/10.1002/adts.202300713>
- (39) B. E. Warren: *X-ray Diffraction*, Dover Publications, New York, (1990), 116–149. ISBN 0-486-66317-5
- (40) P. Debye: *Ann. Phys.*, **351** (1915), 809–823. <https://doi.org/10.1002/andp.19153510606>
- (41) P. Scardi, S. J. L. Billinge, R. Neder and A. Cervellino: *Acta Crystallogr.*, **A72** (2016), 589–590. <https://doi.org/10.1107/S2053273316015680>
- (42) D. P. Olds and P. M. Duxbury: *J. Appl. Cryst.*, **47** (2014), 1077–1086. <https://doi.org/10.1107/S1600576714005925>
- (43) E. Wetterskog, A. Klapper, S. Disch, E. Josten, R. P. Hermann, U. Rücker, T. Brückel, L. Bergström and G. Salazar-Alvarez: *Nanoscale*, **8** (2016), 15571–15580. <https://doi.org/10.1039/C6NR03776C>
- (44) D. Dresen, A. Qdemat, S. Ulusoy, F. Mees, D. Zákutná, E. Wetterskog, E. Kentzinger, G. Salazar-Alvarez and S. Disch: *J. Phys. Chem. C*, **125**, **42** (2021), 23356–23363. <https://doi.org/10.1021/acs.jpcc.1c06082>
- (45) E. P. Barrett, L. G. Joyner and P. P. Halenda: *J. Am. Chem. Soc.*, **73** (1951), 373–380. <https://doi.org/10.1021/ja01145a126>
- (46) K. Momma and F. Izumi: *J. Appl. Cryst.*, **44** (2011), 1272–1276. <https://doi.org/10.1107/S0021889811038970>

Appendix

A. Number Density Function

When creating the number density function ($P(r, \vec{r}_0)$) from the number of particles in the small volume ($\Delta V(r) = 4\pi r^2 \Delta r$) within the radius $r \pm 1/2 \Delta r$, it can be expressed as follows:

$$P(r, \vec{r}_0) = \frac{1}{\Delta V(r)} \sum_n^N P(r, |\vec{r}_n - \vec{r}_0|) \quad (\text{A1})$$

$$p(r, r_{0n}) = \begin{cases} 1 & \text{if } \left(r - \frac{1}{2} \Delta r \right) < r_{0n} \leq \left(r + \frac{1}{2} \Delta r \right) \\ 0 & \text{else} \end{cases} \quad (\text{A2})$$

where \vec{r}_0 is the center of the sphere. The number density function ($\rho(r)$) in the double summation calculations of DSE and mDSE can be expressed as following:

$$\rho(r) = \frac{1}{N} \sum_m^N P(r, r_m) \quad (\text{A3})$$

B. Relative Difference

The difference ($\Delta I(q)$) and the relative difference ($\Delta I(q)/I_{\text{obs}}(q)$) between the simulated intensity ($I_{\text{calc}}(q)$) and the observed intensity ($I_{\text{obs}}(q)$) are defined as follows, respectively:

$$\Delta I(q) = I_{\text{calc}}(q) - I_{\text{obs}}(q) \quad (\text{B1})$$

$$\Delta I(q)/I_{\text{obs}}(q) = \frac{I_{\text{calc}}(q) - I_{\text{obs}}(q)}{I_{\text{obs}}(q)} \quad (\text{B2})$$

In the SAXS pattern of a silica aerogel shown in Fig. 1, the minimum and maximum values of the observed intensity differ by about four orders of magnitude, and the difference $\Delta I(q)$ also differs by orders of magnitude. Therefore, when comparing the observed and simulated intensity, it is easier to understand by using the relative difference ($\Delta I(q)/I_{\text{obs}}(q)$), which is normalized for each q -data point.

C. Coordination Number

We define that a pair of particles are coordinated when they are overlapping with increasing radius multiplied by $(1 + \epsilon)$. The coordination number of catalysis particle C for i_s -th support particle can be expressed as follows:

$$X_{i_s C} = \sum_{j_c}^{N_c} x_{i_s j_c} \quad (C1)$$

$$x_{i_s j_c} = \begin{cases} 1 & \text{if } r_{i_s j_c} \leq (1 + \epsilon)(R_{i_s} + R_{j_c}) \\ 0 & \text{else} \end{cases} \quad (C2)$$

Where R_{i_s} and R_{j_c} are the i_s -th and j_c -th particle radii, respectively. The frequency $Y_{SC}(X)$ of the coordination number X of catalysis particle C for the support particle S can be expressed as follows:

$$Y_{SC}(X) = \frac{1}{N_S} \sum_{i_s}^{N_S} y_{i_s C}(X) \quad (C3)$$

$$y_{i_s C}(X) = \begin{cases} 1 & \text{if } X = X_{i_s C} \\ 0 & \text{else} \end{cases} \quad (C4)$$

$$\sum_{X=0}^{\infty} Y_{SC}(X) = 1 \quad (C5)$$